

Low-voltage and fully flexible analogue/digital mixed-signal circuits based on carbon nanotubes for epidermal sensor applications

Taikga Kashima

Nagoya University

Shigeru Kishimoto

Nagoya University

Jun Hirotani

Nagoya University

Hikomichi Kataura

National Institute of Advanced Industrial Science and Technology

Yutaka Ohno (✉ yohn@nagoya-u.jp)

Nagoya University

Article

Keywords:

Posted Date: September 11th, 2020

DOI: <https://doi.org/10.21203/rs.3.rs-68702/v1>

License:   This work is licensed under a Creative Commons Attribution 4.0 International License.

[Read Full License](#)

1 **Low-voltage and fully flexible analogue/digital mixed-signal**
2 **circuits based on carbon nanotubes for epidermal sensor**
3 **applications**

4 Taiga Kashima¹, Shigeru Kishimoto¹, Jun Hirotsu¹, Hiromichi Kataura², and Yutaka Ohno^{1,3,*}

5 ¹ Department of Electronics, Nagoya University, Furo-cho, Chikusa-ku, Nagoya 464-8603,
6 Japan

7 ² Nanomaterials Research Institute, National Institute of Advanced Industrial Science and
8 Technology, Tsukuba, Ibaraki, 305-8565, Japan

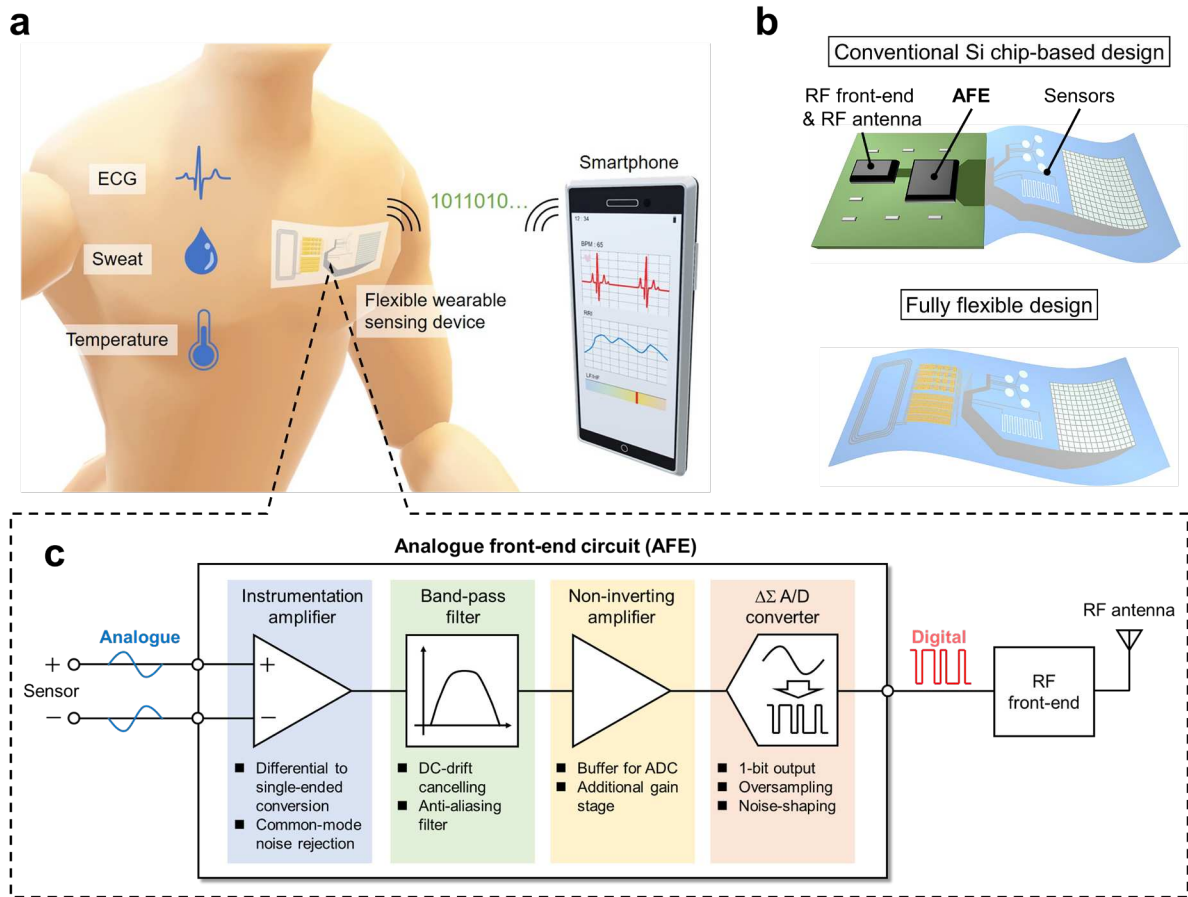
9 ³ Institute of Materials and Systems for Sustainability, Nagoya University, Furo-cho, Chikusa-
10 ku, Nagoya 464-8601, Japan

11 * Corresponding author e-mail: yohno@nagoya-u.jp

12 Epidermal electronics that can be mounted directly onto human skin to monitor biological
13 signals have wide applicability, such as in healthcare and sports. This requires integrating
14 various analogue and analogue/digital mixed-signal circuits on a flexible film as well as sensors.
15 Flexible analogue circuits based on oxide semiconductors or amorphous Si have been realised,
16 but so far they do not allow robust digital signal transmission to an external system, and they
17 have a high operating voltage. Here, we report a low-voltage and fully flexible analogue/digital
18 mixed-signal circuits based on carbon nanotubes (CNTs). The key contribution is a novel
19 operational amplifier with a high gain and low operating voltage, which is important for
20 negative-feedback circuits and dramatically suppresses the influence of device variability and
21 instability. Fully flexible CNT-based mixed-signal circuits were realised monolithically on a
22 plastic film for the first time and demonstrated stable and continuous operation at a low supply
23 voltage.

24 Because flexible wearable sensors can come in close contact with soft human tissue, they are
25 suitable for long-term and non-invasive monitoring of biological signals in a wide range of
26 fields such as medicine, healthcare, and sports (Figure 1a). Intensive research has resulted in
27 the development of epidermal sensors to detect a wide range of biological signals, such as the
28 electrocardiogram (ECG),¹⁻⁴ electromyogram,^{5,6} sweating,^{7,8} body temperature,^{9,10} surface
29 strain,¹¹⁻¹³ and pressure.^{14,15} However, these sensor systems process signals by relying on either
30 a remote information terminal or rigid silicon-based chips placed on the sensor device, which
31 degrades the overall flexibility and durability (Figure 1b). Replacing silicon chips with fully
32 flexible electronics can help realise epidermal devices that provide intimate contact with the
33 human body.

34 To realise an epidermal sensor system, various electronic circuits need to be integrated on a
35 flexible film, including the analogue frontend (AFE) and radiofrequency (RF) frontend (Figure
36 1c). The AFE amplifies and digitises the weak output signal from a sensor. Digital data are
37 transferred to the RF frontend for wireless signal transmission. Flexible AFE circuits based on
38 IGZO¹⁶⁻¹⁸ or amorphous Si¹⁹ have previously been reported, but they were not equipped with
39 an analogue/digital converter (ADC), which is indispensable for robust signal transmission
40 with a high signal-to-noise ratio (SNR) while excluding external noise. In addition, such AFE
41 circuits required high power supply voltages of 10–55 V, which can be attributed to the high
42 operating voltage as well as the variability and instability of their thin-film transistors (TFTs).
43 The power supply voltage for a circuit is generally increased to obtain an operating margin to
44 overcome device variability and instability. However, a low operating voltage is essential for
45 wearable electronics to accommodate safety concerns and a limited power supply.



46

47 **Figure 1 | Fully flexible electronics for epidermal sensors.** (a) Schematic illustration of an
 48 epidermal sensor for monitoring biological signals. (b) Schematic illustrations of a
 49 conventional Si chip-based design and fully flexible design of flexible sensor. (c) Circuit
 50 diagram of the sensor system consisting of a sensor, AFE, and RF frontend. The configuration
 51 of the AFE and roles of each element are also shown.

52 Because TFTs based on carbon nanotubes (CNTs) have relatively high mobility²⁰⁻²² and
 53 excellent mechanical flexibility,^{23,24} they may help realise low-voltage flexible electronics for
 54 wearable devices. However, the electrical characteristics of CNT TFTs may have large device-
 55 to-device variability because of the randomness of the network-like CNT thin film.^{25,26} This
 56 can significantly degrade the performance and increase the operating voltage of CNT-based
 57 circuits compared to the ideal case. In addition, CNT TFTs often exhibit instability issues such
 58 as hysteresis and threshold voltage drift under a bias stress. Addressing these issues is the most

59 important challenge for realising high-performance CNT-based flexible electronics, especially
60 analogue circuits that require high stability.

61 We developed a methodology to realise low-voltage CNT-based flexible analogue/digital
62 mixed-signal circuits with excellent stability and robustness against variability. A novel
63 backside exposure self-aligned (BESA) process was developed for fabricating flexible CNT
64 TFTs on a transparent plastic film, which minimises the parasitic capacitance and hence the
65 delay time. We developed a device model and simulation tools for CNT-based analogue and
66 digital mixed-signal circuits. The key circuit is a novel operational amplifier (op-amp) with a
67 high gain and low operating voltage; this is important for the construction of negative-feedback
68 circuits, which can dramatically suppress the influence of device variability and instability on
69 the circuit performance. A bending test was conducted to demonstrate the excellent flexibility
70 of the developed circuits. A flexible delta-sigma ADC with high energy efficiency was also
71 realised. We used the above results to realise a fully flexible CNT AFE for the first time that
72 monolithically integrates an instrument amplifier, bandpass filter, non-inverting amplifier, and
73 delta-sigma ADC on a plastic film. In experiments, it demonstrated stable and continuous
74 operation during the amplification and digitalisation of ECG signals. All flexible analogue and
75 mixed-signal circuits fabricated in this work could be operated at a low supply voltage of ± 1.5
76 V.

77 **BESA process for flexible CNT TFTs**

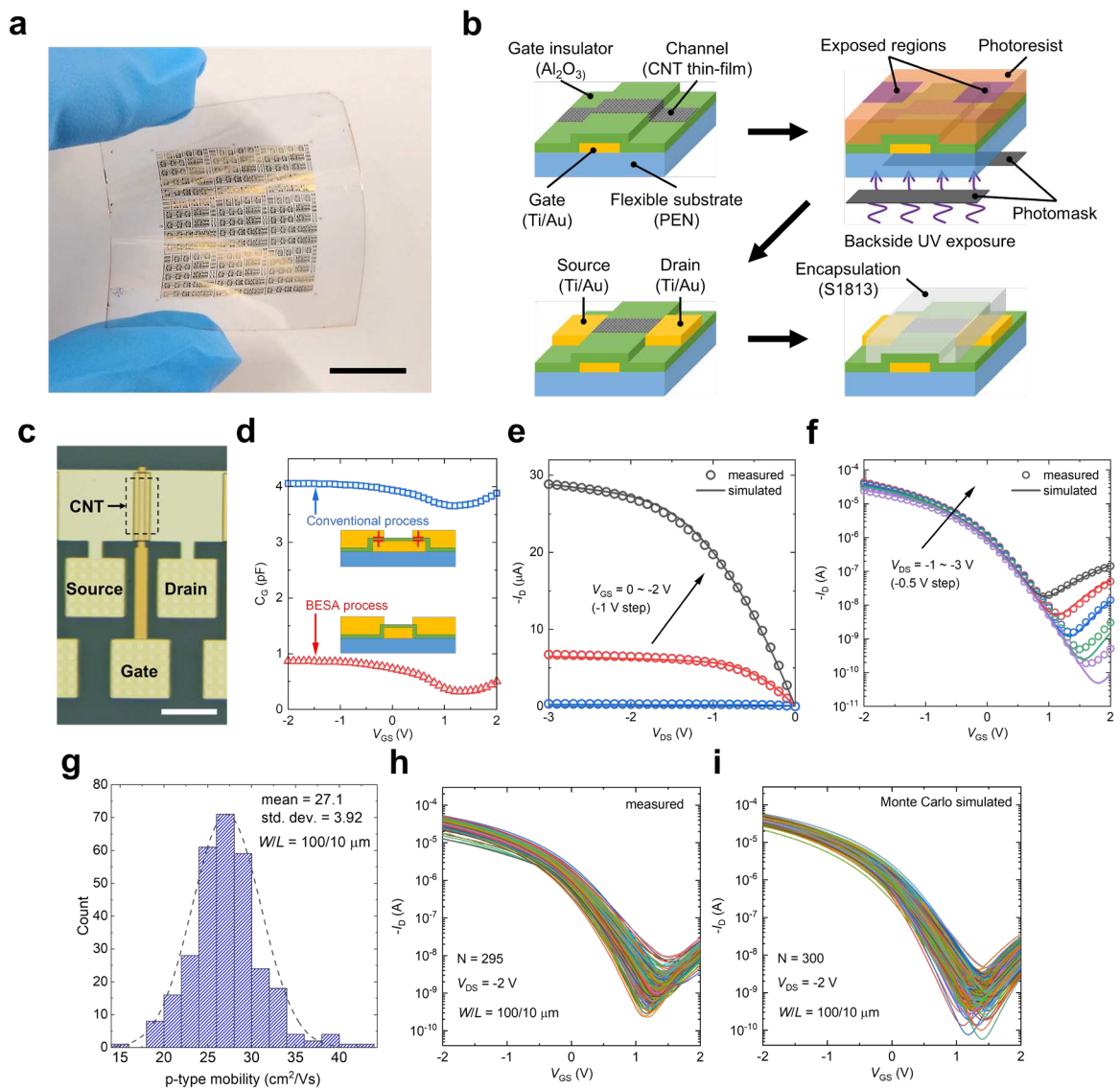
78 The self-aligned process is essential to reduce parasitic capacitance and improve the operating
79 speed of CNT TFTs, particularly those fabricated on a flexible plastic film. Because such films
80 slightly shrink during the device fabrication process, a large margin is required for layer-to-
81 layer alignment. For example, a margin of 20 μm is necessary to account for 0.1% shrinkage
82 of a $20 \times 20 \text{ mm}^2$ plastic film. Consequently, a large parasitic capacitance forms because of the
83 overlap between the gate and source/drain electrodes. We developed the BESA process by

84 utilising the transparency of the plastic film so that the source/drain electrodes self-align to the
85 gate. Figures 2a and 2b show CNT TFTs that were fabricated on a flexible and transparent
86 polyethylene naphthalate (PEN) film with the BESA process. The BESA process took place
87 during the lithography process for the source/drain formation; ultraviolet (UV) light was
88 exposed from the backside of the PEN substrate through a photomask and gate electrode, which
89 minimised the overlap between the gate and source/drain electrodes.

90 Figure 2c shows a micrograph of a CNT TFT fabricated by the BESA process ($W/L = 100/10$
91 μm). The overlap between the gate and source/drain is difficult to recognise. Figure 2d shows
92 the measured gate capacitance (C_G)–gate voltage (V_{GS}) relationship. The parasitic capacitance
93 due to the overlap can be observed in the off state of the p -type channel ($V_{GS} > 1$ V). The off-
94 state of the BESA-based CNT TFT was 0.32 pF, which was about one-eleventh of that for the
95 conventionally fabricated device with a 10- μm overlap (3.65 pF). This demonstrated the
96 effectiveness of the BESA process. The BESA process is also quite simple and reliable
97 compared to the conventional self-aligned process.²⁷ There was no device failure related to the
98 BESA process, which indicates its suitability for application to large-area flexible integrated
99 circuits (ICs) requiring a high performance level.

100 Figures 2e and 2f show the output and transfer characteristics, respectively, of a CNT TFT.
101 The device exhibited typical p -type characteristics, and the mobility was estimated from the
102 transconductance and C_G in the on state to have a maximum value of 42.7 cm^2/Vs and average
103 of 27.1 cm^2/Vs . These are comparable to the results of previous reports.^{28–30} For the circuit
104 design in HSPICE, we developed a CNT TFT model by modifying a previous model³¹ for
105 simulating devices operating in a deep off region, where minority carrier conduction occurs.
106 The current model fit the experimental data well (solid curves in Figures 2e and 2f). To obtain
107 the C_G – V_{GS} characteristics, we applied the Meyer model often used for organic TFTs³¹ (see the
108 Supplementary Information for details on modelling CNT TFTs).

109 Modelling the variability of CNT TFTs is indispensable for the design of reliable analogue
 110 circuits, whose performance can be seriously affected by device variability. The device
 111 characteristics were statistically analysed to extract model parameters such as the mobility,
 112 threshold voltage, and oxide capacitance (see Supplementary Table S1). The Monte Carlo
 113 method was used for the circuit simulation to account for device variability. The Monte Carlo
 114 method (Figure 2i) closely reproduced the variability of the measured device characteristics
 115 (Figure 2h).



116

117 **Figure 2 | Flexible CNT TFTs fabricated with the BESA process. (a) Photograph of devices**

118 **fabricated on a PEN film. The scale bar is 1 cm. (b) Schematic illustration of the device**

119 fabricated with the BESA process. (c) Photograph of a CNT TFT. (d) C_G - V_{GS} characteristics
120 of CNT TFTs fabricated by the conventional process and BESA process. (e) I_D - V_{DS} and (f) I_D -
121 V_{GS} characteristics of a typical CNT TFT. (g) Histogram of carrier mobility. The broken curve
122 is the Gaussian fit. The mean value and standard deviation were 27.1 and 3.92 cm^2/Vs . (h)
123 Measured and (i) simulated I_D - V_{GS} characteristics of CNT TFTs at $V_{DS} = -2$ V.

124 **Design and fabrication of high-gain and low-voltage op-amp**

125 A differential amplifier is often used for the first stage of the AFE to amplify weak sensor
126 signals. However, the amplification characteristics easily fluctuate because of the variability
127 and instability in the electrical properties of transistors. The key to solving the problem of
128 device variability is a negative-feedback circuit based on an op-amp. If the open-loop gain of
129 the op-amp is sufficiently high, then the amplification characteristics will be determined by
130 externally connected passive elements such as resistors and capacitors. Op-amps are also an
131 important core circuit often used in various functional circuits such as instrument amplifiers
132 and ADCs in the AFE and other analogue/digital mixed-signal circuits.

133 Figure 3a shows a typical two-stage CMOS-based op-amp that can provide a high gain with
134 relatively few transistors. However, this circuit configuration is sensitive to device variability,
135 which can cause an input offset voltage (V_{OS}). In the ideal case, V_{OS} is zero; however, it
136 becomes significant when paired transistors have mismatched characteristics. For example,
137 $M_1:M_2$ or $M_3:M_4$ in Figure 3a limits the output swing and gain at a low operating voltage. This
138 issue is particularly serious for op-amps using CNT TFTs, which have large variability. To
139 solve this issue, we propose a novel op-amp circuit comprising single-polarity transistors
140 (Figure 3b) that has excellent robustness against device variability and requires a low operating
141 voltage.

142 Figure 3c shows a schematic of V_{OS} and its influence on the dynamic range of a non-inverting
143 amplifier, which comprises two resistors and a CMOS-based op-amp or the proposed op-amp.

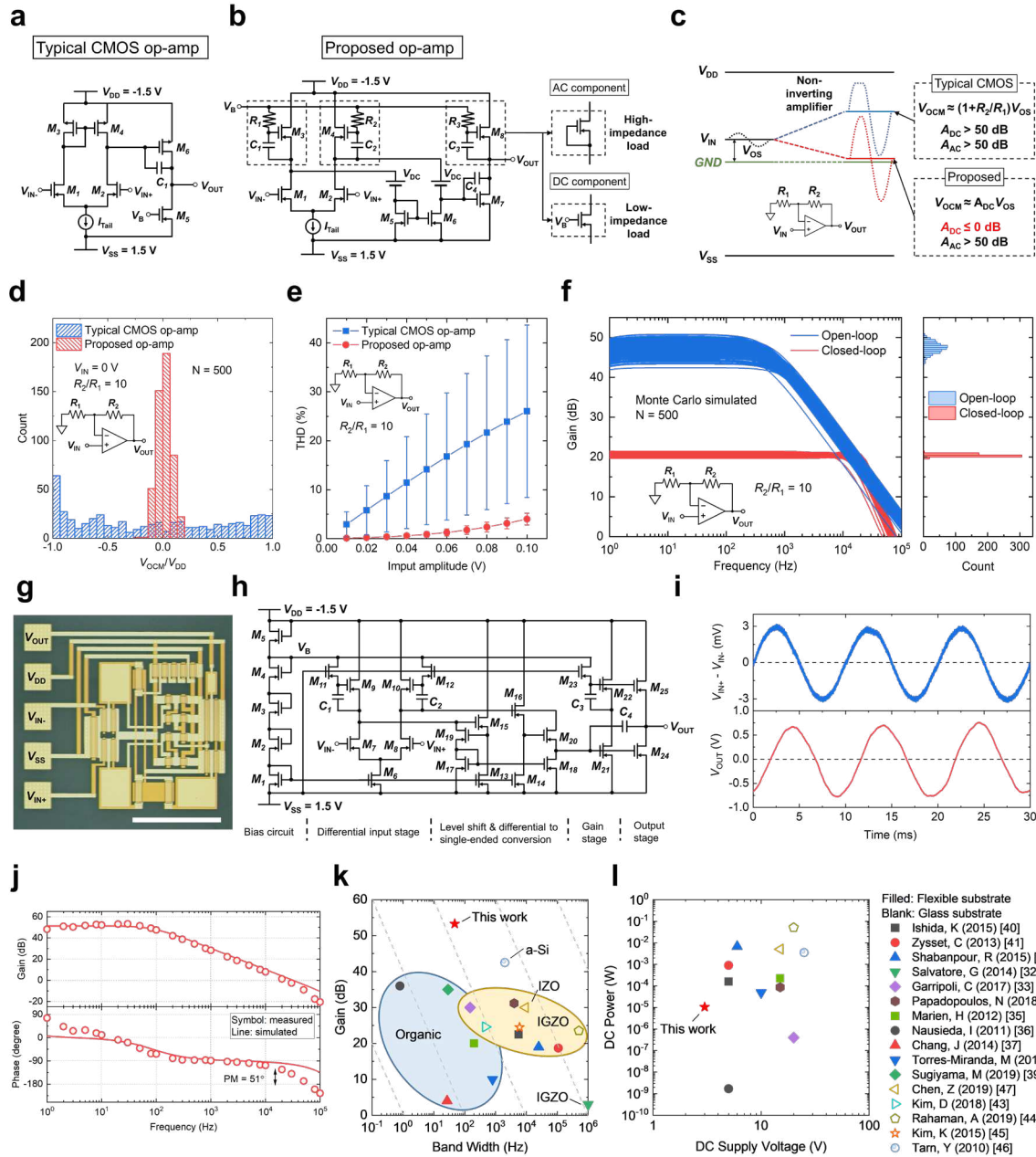
144 The input voltage (V_{IN}) consists of the AC input signal and additional DC offset voltage due to
145 V_{OS} . With the CMOS-based op-amp, both the AC signal and V_{OS} are amplified by an
146 amplification factor of approximately $1 + R_2/R_1$ because both the AC voltage gain (A_{AC}) and
147 DC voltage gain (A_{DC}) of the op-amp are relatively high (typically >50 dB). This causes a large
148 offset voltage at the output called the common-mode output voltage (V_{OCM}), and the output
149 voltage swing is limited. Therefore, the output voltage waveform is likely to be distorted at a
150 low supply voltage when A_{AC} is high. In other words, device variability results in a trade-off
151 between a low operating voltage and high gain with the CMOS-based op-amp.

152 In contrast, the proposed op-amp can overcome this trade-off, even for CNT TFTs. The key to
153 the proposed op-amp is independent control of A_{AC} and A_{DC} . It achieves a high A_{AC} of >50 dB
154 and small A_{DC} below unity simultaneously. The AC-coupled load consisting of a transistor and
155 a capacitor (surrounded with broken lines in Figure 3b) has a high/low impedance for the
156 AC/DC component. The optimal V_B should realise a high $A_{AC} = 48$ dB and small $A_{DC} = -4.8$
157 dB. See the Supplementary information for the details.

158 The proposed circuit configuration has several advantages with regard to tolerance to
159 variability in the transistor characteristics. We performed a Monte Carlo simulation to
160 investigate the influence of the transistor variability on the non-inverting amplifier circuit.
161 Figure 3d shows the V_{OCM} distributions of non-inverting amplifiers comprising the proposed
162 op-amp or CMOS op-amp. With the CMOS op-amp, V_{OCM} scattered widely from $V_{SS}(= -V_{DD})$
163 to V_{DD} because of transistor variability. This eventually caused a large total harmonic distortion
164 (THD) of the output signal (Figure 3e). In contrast, the proposed op-amp caused V_{OCM} to
165 converge around zero. Consequently, the THD of the non-inverting amplifier was effectively
166 suppressed, even when the variability in the transistor characteristics was accounted for. A low
167 THD is particularly important for sensor applications that require a linear detection response.
168 We confirmed that the proposed op-amp suppresses the variability in characteristics of a

169 negative-feedback circuit. Figure 3f shows the open-loop voltage gain of the proposed op-amp
170 and closed-loop voltage gain of a non-inverting amplifier with the op-amp as a function of
171 frequency. Even for the open-loop voltage gain, a relatively narrow distribution was obtained
172 because of the small V_{OCM} . A high open-loop gain is essential for proper operation of a
173 negative-feedback circuit. The variability was drastically suppressed with the non-inverting
174 amplifier circuit. Although we considered the static variability of transistor characteristics in
175 this simulation, a negative-feedback circuit is also effective at suppressing the influence of
176 electrical instability and drift in transistor characteristics, which are often observed for CNT
177 TFTs.

178



179

180 **Figure 3 | Design and fabrication of the high-gain and low-voltage op-amp with high**
 181 **tolerance to transistor variability.** (a) Circuit configuration of a typical two-stage CMOS-
 182 based op-amp. (b) Circuit configuration of the proposed op-amp. (c) Schematics of the voltage
 183 levels of V_{OS} and V_{OCM} for non-inverting amplifiers composed of the CMOS-based op-amp and
 184 proposed op-amp, respectively. The inset shows the circuit configuration of the non-inverting
 185 amplifier. Results of the Monte Carlo simulations of op-amps: (d) V_{OCM} distribution normalised
 186 by V_{DD} , (e) THD as a function of the input voltage amplitude of non-inverting amplifiers

187 composed of the CMOS op-amp and proposed op-amp, and (f) open-loop voltage gain of the
188 proposed op-amp and closed-loop voltage gain of the non-inverting amplifier composed of the
189 proposed op-amp as functions of the frequency and the maximum gain distributions. (g)
190 Photograph of the fabricated flexible CNT op-amp. The scale bar is 500 μm . (h) Circuit
191 diagram of the CNT op-amp. (i) Input (upper) and output (bottom) voltage waveforms. (j)
192 Fabrication and characterisation of the CNT op-amp. (k) Voltage gain versus bandwidth and
193 (l) DC power versus DC supply voltage of the present CNT op-amp and the differential
194 amplifiers and op-amps reported previously for comparison.

195 A flexible op-amp based on CNT TFTs was fabricated on a PEN film (Figures 3g and 3h) that
196 fully integrates the circuits necessary to realise the proposed design described in the previous
197 section: the bias circuit, differential input stage, level shift and differential-to-single-end
198 converter, gain stage, and output stage. No additional bias voltage is necessary to control the
199 bias point of the TFTs. See the Supplementary Information for the details of the op-amp circuit.

200 Figure 3i shows the voltage waveforms of the sinusoidal input ($V_{\text{IN}+} - V_{\text{IN}-}$) and V_{OUT} at 100
201 Hz. The power supply voltages were $V_{\text{DD}} = -1.5 \text{ V}$ and $V_{\text{SS}} = +1.5 \text{ V}$. The amplitude of the
202 output voltage was 1.4 V_{pp} for an input voltage of 6 mV_{pp} , which indicated a high open-loop
203 gain of 47.4 dB at 100 Hz. Figure 3j shows the open-loop gain and phase as a function of the
204 frequency. The gain in the low-frequency region was 53.3 dB, and the bandwidth and unity-
205 gain frequency were 47.5 and 21.9 kHz, respectively. The phase margin, which could be
206 controlled by the phase compensation capacitor C_4 , was 51° . This large phase margin is
207 sufficient for stable operation of a negative-feedback circuit without oscillation. Importantly,
208 the measured characteristics of the fabricated op-amp (open circles in Figure 3j) showed good
209 agreement with our simulation results (solid curves), which indicates a high degree of
210 completion for the device model and circuit design tools.

211 We compared the performance of the present CNT op-amp with those of various differential
212 amplifiers^{32–39} and op-amps:^{40–46} single-polarity TFTs on a flexible substrate^{32–42} or glass
213 substrate^{43–47} and with oxide semiconductors,^{32–34,40–45,47} organic semiconductors,^{35–39} or
214 amorphous Si⁴⁶. The present op-amp clearly had the highest voltage gain (Figure 3k), which
215 was because of the proposed AC-coupling load circuit configuration. Most of the previous
216 differential amplifiers and op-amps had a gain of less than 30 dB, which is insufficient for
217 negative-feedback circuits. The present op-amp had a higher gain-bandwidth product than
218 those based on organic semiconductors and comparable with those based on oxide
219 semiconductors.

220 The present op-amp could operate at a low supply voltage of ± 1.5 V, which can be supplied by
221 lithium-ion batteries. It had the lowest operating voltage (Figure 3i), which led to a low power
222 consumption of 10.5 μ W. The low operating voltage and power consumption demonstrate the
223 advantages of the CNT-based flexible op-amp for wearable device applications with regard to
224 safety and limited power sources (see Supplementary Table S3).

225 **Negative-feedback circuits**

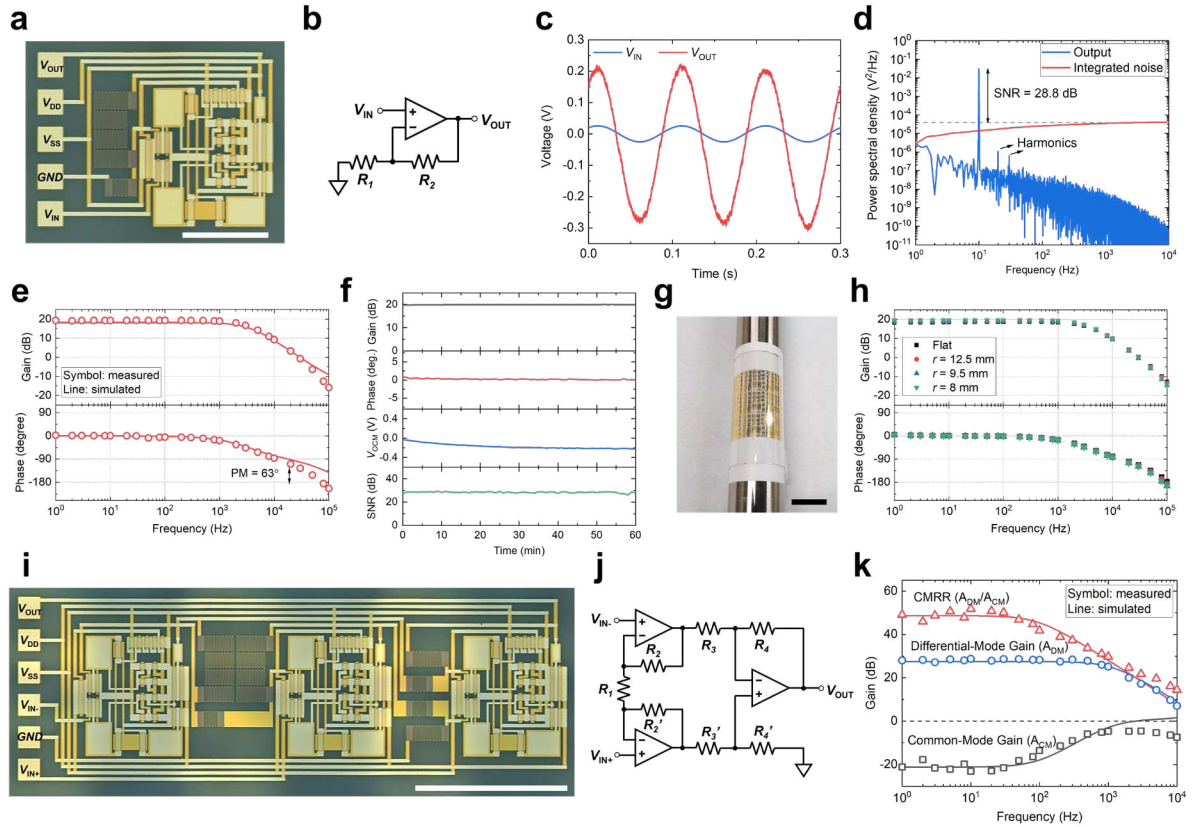
226 The greatest benefit of the present high-gain op-amp is the negative-feedback circuit, which
227 provides various analogue functional circuits with better stability, reliability, and uniformity
228 than other types of amplifier circuits. Here, we present a non-inverting amplifier and
229 instrumentation amplifier; both are key components for constructing an AFE.

230 The non-inverting amplifier fabricated on a PEN film (Figures 4a and 4b) was driven at power
231 supply of ± 1.5 V. (See the Supplementary Information for the details.) Figure 4c shows the
232 output voltage waveform for a sinusoidal voltage wave input at 10 Hz. The output voltage
233 exhibited an amplified sine wave without distortion. The voltage gain was 19.5 dB, which is
234 close to the design value of 19.1 dB (4.8% difference). The linearity was confirmed by the
235 measured spectrum of the output voltage (Figure 4d). The power densities of the second and

236 third harmonics were negligible at -44.6 and -46.9 dB relative to the fundamental wave, and
237 the THD was 0.8%. The measured SNR was 28.8 dB, which is greater than the 25 dB required
238 for ECG application.⁴⁸ The bandwidth of the non-inverting amplifier was 2.46 kHz with a
239 sufficient phase margin of 63° (Figure 4e); this is also sufficient for monitoring various bio-
240 signals. The stability of the non-inverting amplifier was also investigated. Figure 4f shows the
241 changes in the gain, phase, V_{OCM} , and SNR over a time of 1 h. The gain, phase, and SNR are
242 fundamental performance indices of an amplifier and indicated excellent stability. The change
243 in V_{OCM} was small at 6.7% of the power supply voltage, which would not affect the amplifier
244 performance. We examined the stability of the amplification characteristics against bending at
245 various bending radii (r) of 12.5, 9.5, and 8.0 mm (Figure 4g). The non-inverting amplifier
246 exhibited almost no changes in the gain (<1 dB) and phase at $r = 8.0$ mm (Figure 4h).

247 An instrumentation amplifier was also fabricated on a PEN substrate (Figures 4i and 4j) and
248 consisted of three op-amps. One of the roles of an instrumentation amplifier in a sensor system
249 is to reject common-mode signals, which normally originate from noise. In contrast, a
250 differential-mode signal originates from a sensor signal. The common-mode rejection ratio
251 (CMRR) is an important performance index for instrumentation amplifiers and is given by
252 $CMRR = A_{DM} / A_{CM}$, where A_{DM} and A_{CM} are the differential- and common-mode gains,
253 respectively (see the Supplementary Information for measuring $CMRR$). A high CMRR of ~ 50
254 dB was obtained in the present instrumentation amplifier (Figure 4k), so excellent noise
255 reduction can be expected.

256 The experimentally measured characteristics showed good agreement with the simulation
257 results for both the non-inversion amplifier and instrumentation amplifier (Figures 4g and 4i,
258 respectively). This clearly demonstrates the reliability of the proposed circuit design technique
259 and reproducibility of the device fabrication.



260

261 **Figure 4 | Negative-feedback circuits composed of CNT op-amps. Non-inverting amplifier:**

262 (a) photograph (scale bar: 500 μm), (b) circuit diagram, (c) input and output voltage waveform,

263 (d) power spectral density as a function of frequency, (e) measured (open circle) and simulated

264 (solid curve) gain (upper) and phase (bottom) as a function of frequency, and (f) changes in the

265 gain, phase, V_{OCM} , and SNR (from top to bottom) for 1 h. (g) Photograph of the bending test

266 (scale bar: 1 cm), and (h) gain and phase as a function of frequency under various bending

267 condition. Instrumentation amplifier: (i) photograph, (j) circuit diagram, and (k) CMRR, A_{DM} ,

268 and A_{CM} as a function of frequency.

269 Design and fabrication of a delta-sigma type ADC

270 ADCs are an important component for robust signal transfer from a sensor system to an

271 information processing terminal. We designed a switched-capacitor (SC) delta-sigma ($\Delta\Sigma$)

272 ADC that can comprise relatively few transistors and operate with low power consumption

273 (Figures 5a and 5b). The $\Delta\Sigma$ ADC is advantageous for sensor applications because of the high

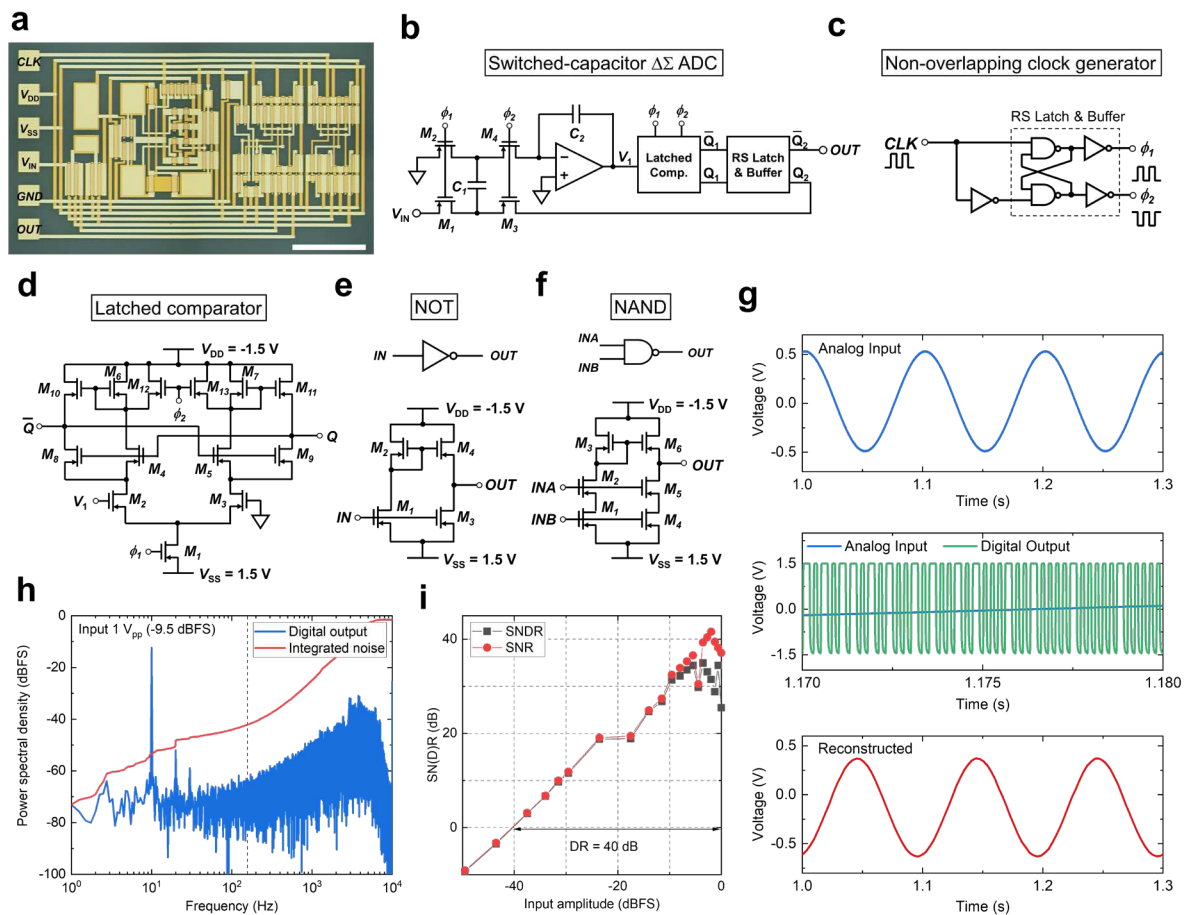
274 SNR in a low-frequency region from noise-shaping behaviour.

275 The fabricated ADC comprises a non-overlapping clock generator (Figure 5c), SC integrator,
276 latched comparator (Figure 5d), RS latch, and buffer. The pseudo complementary metal–
277 oxide–semiconductor (CMOS) technique⁴⁹ is useful for improving the operating speed and
278 noise margin of digital ICs comprising single-polarity transistors and was introduced in the
279 digital gates such as latched comparator, NOT (Figure 5e), and NAND (Figure 5f). $\Delta\Sigma$ ADC
280 outputs a 1-bit pulse density modulation signal that depends on the input voltage. See the
281 Supplementary Information for the details of the operation.

282 The CNT-based flexible ADC was successfully operated at a power supply voltage of ± 1.5 V,
283 clock frequency (CLK) of 10 kHz, oversampling rate (OSR) of 32, and signal bandwidth of
284 156 Hz (Figure 5g). When the analogue input was a sine wave at 10 Hz and 1 V_{pp}, the pulse
285 density of the digital output increased with the analogue input voltage. The digital output was
286 reconverted to an analogue signal by a finite impulse response (FIR) decimation filter with a
287 decimation rate of 32 on a PC. The sinusoidal signal was confirmed as reconstructed without
288 distortion.

289 Figure 5h shows the power spectral density (PSD) of the digital output. The noise-shaping
290 behaviour characteristic of $\Delta\Sigma$ ADCs was observed above ~ 200 Hz, so the noise level in the
291 signal region (< 200 Hz) was effectively reduced. The SNR and signal-to-noise distortion ratio
292 (SNDR) are shown in Figure 5i as functions of the input amplitude. A high SNR of 42 dB and
293 SNDR of 35 dB were obtained. The dynamic range (DR) was estimated to be 40 dB from the
294 ratio of the maximum input amplitude to the input amplitude to give SNR = 0 dB. The effective
295 number of bits (ENOB) was determined to be 5.5 bit. The energy efficiency, which is
296 commonly used as a figure of merit of ADCs, was estimated to be 2.06 nJ/conv.step from the
297 ENOB, bandwidth, and power consumption of 29.1 μ W (see the Supplementary Information).
298 The energy efficiency was one to two orders of magnitude better than those reported previously

299 for flexible ADCs (see Supplementary Table S4). The excellent energy efficiency resulted from
 300 the high carrier mobility and low operating voltage of CNT TFTs and demonstrated the
 301 advantage of CNT-based flexible electronics.



302
 303 **Figure 5 | Flexible CNT ADC.** (a) Photograph (Scale bar: 500 μm) and (b) circuit diagram of
 304 SC $\Delta\Sigma$ ADC fabricated in this study. Circuit diagrams of the (c) non-overlapping clock
 305 generator, (d) latched capacitor, (e) NOT gate, and (f) NAND gate. (g) Input voltage (top),
 306 analogue input voltage and digital output voltage on a magnified time scale (middle), and
 307 analogue signal reconstructed from the digital output (bottom). (h) PSD and integrated noise
 308 level of the digital output as a function of the DR of the frequency. (i) SNR and SNDR versus the input
 309 voltage amplitude.

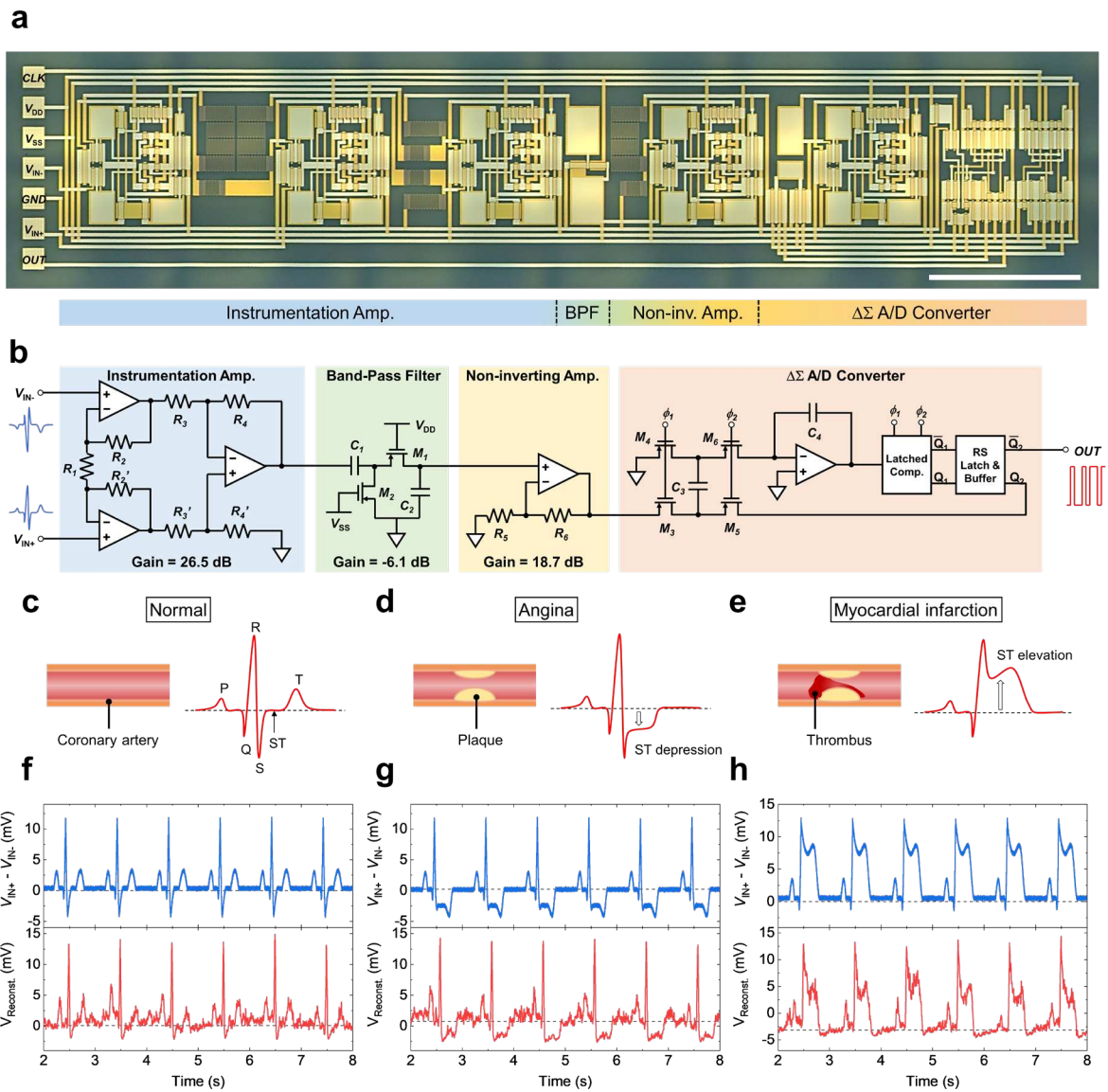
310 **ECG signal monitoring with fully integrated flexible AFE**

311 One of the most important applications of wearable flexible sensors is monitoring bio-signals.
312 For example, the ECG can be used not only to indicate exercise intensity and stress but also to
313 diagnose various diseases such as arrhythmia and angina pectoris. We realised a CNT-based
314 fully flexible AFE and demonstrated its feasibility and advantages for application as a wearable
315 ECG device.

316 The fabricated AFE consists of an instrumentation amplifier, bandpass filter, non-inverting
317 amplifier, and SC $\Delta\Sigma$ ADC (Figures 6a and 6b). All components were monolithically integrated
318 on a flexible plastic film. The CNT-based flexible AFE could also operate at a low supply
319 voltage of ± 1.5 V with a power consumption of 150 μ W. We applied a simulated ECG signal
320 with an amplitude of 16 mV_{pp} to the AFE and then reconstructed the ECG signal on a PC from
321 the collected digital data.

322 Figure 6c shows a schematic for the coronary artery of a healthy person and the ECG with a
323 normal sinus rhythm. PQRST reflects the depolarisation and repolarisation of the heart's atria
324 and ventricles, and the ST segment (i.e. flat region between the S and T waves) coincides with
325 the baseline. Figure 6f shows the simulated ECG applied to the AFE as an input signal and the
326 reconstructed waveform from the digital output. P- and T-wave peaks as well as the R-R
327 intervals corresponding to the heart rate can be observed in the reconstructed ECG.

328 Abnormal ECGs can also be distinguished. For example, an angina occurs when cholesterol
329 builds up and plaque forms in the coronary arteries. In this case, the ST segment of the ECG
330 waveform is known to be lower than the baseline (Figure 6d). If a blood clot forms in a coronary
331 artery, a myocardial infarction occurs. This is reflected in the ECG by an elevation in the ST
332 segment (Figure 6e). These characteristic behaviours of the ST segment can be seen in the
333 reconstructed waveforms (Figures 6g and 6h). We also confirmed that the AFE could operate
334 continuously for at least 1 h (see Supplementary Figure S6). These results demonstrate that the
335 CNT-based flexible AFE provides sufficient resolution to diagnose diseases from weak bio-



337

338 **Figure 6 | CNT-based fully flexible AFE.** (a) Photograph (scale bar: 1 mm) and (b) block
 339 diagram. Schematics of the coronary artery and ECG waveforms indicating (c) normal
 340 conditions, (b) an angina, and (c) a myocardial infarction (c). Input voltage waveforms to the
 341 AFM (upper) and reconstructed voltage waveforms from the digital output data (bottom)
 342 indicating (f) normal conditions, (g) an angina, and (h) a myocardial infarction.

343 **Conclusion**

344 We developed a method for realising CNT-based flexible analogue circuits with excellent

345 tolerance of variability and stability while requiring a low power consumption. A CNT op-amp
346 with high gain and high tolerance of device variation was developed with an AC-coupled load
347 circuit configuration and bias circuit to enhance A_{AC}/A_{DC} , which drastically suppresses the
348 variability of V_{OCM} . We also developed a BESA process to minimise the parasitic capacitance,
349 which causes excess delay in CNT TFTs. The developed CNT op-amp realised a very high
350 voltage gain of 53.3 dB at a low supply voltage of ± 1.5 V, which enabled the design of a stable
351 circuit system with negative feedback control. For example, a non-inverting amplifier was
352 developed that exhibited stable operation for at least 1 h. We also developed an instrumentation
353 amplifier with a high CMRR of 50 dB, which demonstrates excellent noise reduction
354 performance. A fully flexible AFE was monolithically integrated on a flexible plastic film; it
355 exhibited an excellent energy efficiency of 2.06 nJ/conv.step, and it successfully converted a
356 weak ECG signal of 16 mVpp to robust digital data. Abnormal ST signals could be
357 distinguished in the ECG waveform reconstructed from the digital output.

358 Our results clearly demonstrate the advantages of CNT-based flexible analogue and
359 analogue/digital mixed-signal circuits; the low voltage and power consumption are particularly
360 important for realising wearable and epidermal sensor systems. In the future, low-voltage CNT-
361 based flexible electronics may pave the way to realising self-powered epidermal sensor systems
362 equipped with energy harvesters.

363 **Methods**

364 *Device fabrication process*

365 CNT TFTs and ICs were fabricated on a 125- μ m-thick PEN film. Gate electrodes of Ti/Au
366 (1/50 nm) were formed by conventional photolithography, electron beam evaporation, and the
367 lift-off process. Resistors were similarly formed by depositing 20-nm-thick nichrome. A 60-
368 nm-thick Al_2O_3 gate insulator was formed by atomic layer deposition at 140 °C. Then, contact
369 windows were opened by CF_4 plasma reactive ion etching of Al_2O_3 . The semiconductor CNT

370 thin film was formed by the transfer process as reported previously,²⁵ followed by oxygen
371 plasma etching. Source and drain electrodes of Ti/Au (0.4/50 nm) were formed by the BESA
372 process. The device was completed by encapsulation with a photoresist (Shipley, Microposit
373 S1813) layer followed by baking at 130 °C for 20 min.

374 *Electrical measurements*

375 All electrical measurements were carried out under ambient conditions. The I - V and C - V
376 characteristics of the CNT TFTs were measured by an automatic probe station (Hisol, HSP-
377 100) with a semiconductor device parameter analyser (Keysight, B1500A). The CNT ICs were
378 also characterised by the automatic probe station. The input voltage signal was generated by a
379 function generator (Tektronics, AFG1062). A clock signal was applied from another function
380 generator (Agilent, 33250A), and the output signal was measured with a digital oscilloscope
381 (Tektronics, MOS58). In the durability test against bending, samples were bent by being
382 attached to a rod with a diameter of 16, 19, or 25 mm and set on the probe station for electrical
383 measurements.

384 *Device modelling and circuit simulation*

385 The device model for the CNT TFTs was developed from the measured electrical
386 characteristics. The model parameters were extracted by fitting the measured characteristics to
387 the model functions with Origin Pro (OriginLab) following the procedure reported by Deen *et*
388 *al.*⁵⁰ The mean and standard deviation of the model parameters were statistically obtained from
389 the data of 300 devices (see the Supplementary Information). The device model was described
390 with Verilog-A to include the HSPICE simulation. All circuit simulations such as transient,
391 DC, and AC analyses and the Monte Carlo simulations were performed with HSPICE. In the
392 CMOS circuit simulations, we assumed the parameters of the n-type device as equal to those
393 of the p-type device.

394 *Reconstruction of analogue signal from digital data*

395 The output digital signal was measured and recorded by the digital oscilloscope in the comma-
396 separated values (CSV) data format. The digital data were transferred to a PC and converted to
397 an analogue signal through the FIR decimation filter programmed on Simulink in MATLAB
398 (MathWorks).

399 *Generation of ECG signals*

400 ECG waveforms were generated with an arbitral waveform generator (ArbExpress, Tektronics)
401 and transferred to the function generator (AFG1062, Tektronics) to output the differential
402 voltage of the ECG signal.

403 **Data availability**

404 The data that support the findings of this study are available from the corresponding author
405 upon reasonable request.

406

407 **References**

- 408 1. Kim, Y. S. *et al.* All-in-one, wireless, stretchable hybrid electronics for smart, connected,
409 and ambulatory physiological monitoring. *Adv. Sci.* **6**, 1900939 (2019).
- 410 2. Liu, Y. *et al.* Epidermal mechano-acoustic sensing electronics for cardiovascular
411 diagnostics and human-machine interfaces. *Sci. Adv.* **2**, e1601185 (2016).
- 412 3. Khan, Y. *et al.* Flexible hybrid electronics: Direct interfacing of soft and hard electronics
413 for wearable health monitoring. *Adv. Funct. Mater.* **26**, 8764–8775 (2016).
- 414 4. Yamamoto, Y. *et al.* Printed multifunctional flexible device with an integrated motion
415 sensor for health care monitoring. *Sci. Adv.* **2**, e1601473 (2016).
- 416 5. Xu, B. *et al.* An epidermal stimulation and sensing platform for sensorimotor prosthetic
417 control, management of lower back exertion, and electrical muscle activation. *Adv.*
418 *Mater.* **28**, 4462–4471 (2016).
- 419 6. Jeong, J. W. *et al.* Materials and optimized designs for human-machine interfaces via
420 epidermal electronics. *Adv. Mater.* **25**, 6839–6846 (2013).
- 421 7. Lee, H. *et al.* A graphene-based electrochemical device with thermoresponsive
422 microneedles for diabetes monitoring and therapy. *Nat. Nanotechnol.* **11**, 566–572
423 (2016).
- 424 8. Gao, W. *et al.* Fully integrated wearable sensor arrays for multiplexed in situ
425 perspiration analysis. *Nature* **529**, 509–514 (2016).
- 426 9. Ren, X. *et al.* A low-operating-power and flexible active-matrix organic-transistor
427 temperature-sensor array. *Adv. Mater.* **28**, 4832–4838 (2016).
- 428 10. Gao, L. *et al.* Epidermal photonic devices for quantitative imaging of temperature and
429 thermal transport characteristics of the skin. *Nat. Commun.* **5**, 1–10 (2014).
- 430 11. Nur, R. *et al.* A highly sensitive capacitive-type strain sensor using wrinkled ultrathin
431 gold films. *Nano Lett.* **18**, 5610–5617 (2018).

- 432 12. Yamada, T. *et al.* A stretchable carbon nanotube strain sensor for human-motion
433 detection. *Nat. Nanotechnol.* **6**, 296–301 (2011).
- 434 13. Lee, H., Seong, B., Moon, H. & Byun, D. Directly printed stretchable strain sensor based
435 on ring and diamond shaped silver nanowire electrodes. *RSC Adv.* **5**, 28379–28384
436 (2015).
- 437 14. Lee, S. *et al.* A transparent bending-insensitive pressure sensor. *Nat. Nanotechnol.* **11**,
438 472–478 (2016).
- 439 15. Dagdeviren, C. *et al.* Conformable amplified lead zirconate titanate sensors with
440 enhanced piezoelectric response for cutaneous pressure monitoring. *Nat. Commun.* **5**,
441 1–10 (2014).
- 442 16. Garripoli, C., Abdinia, S., van der Steen, J.-L. J. P., Gelinck, G. H. & Cantatore, E. A
443 fully integrated 11.2-mm² a-IGZO EMG front-end circuit on flexible substrate achieving
444 up to 41-dB SNR and 29-M Ω input impedance. *IEEE Solid-State Circuits Lett.* **1**, 142–
445 145 (2018).
- 446 17. Zulqarnain, M. *et al.* A low power time domain ECG interface based on flexible a-IGZO
447 TFTs. in *2019 IEEE 8th International Workshop on Advances in Sensors and Interfaces*
448 *(IWASI), Otranto, Italy, 13–14 June 2019*, 205–209 (IEEE, 2019).
- 449 18. Zulqarnain, M. *et al.* A 52 μ W heart-rate measurement interface fabricated on a flexible
450 foil with a-IGZO TFTs. in *IEEE 44th European Solid State Circuits Conference*
451 *(ESSCIRC), Dresden, Germany, 3–6 September 2018*, 126–129 (IEEE, 2018).
- 452 19. Moy, T. *et al.* An EEG acquisition and biomarker-extraction system using low-noise-
453 amplifier and compressive-sensing circuits based on flexible, thin-film electronics.
454 *IEEE J. Solid-State Circuits* **52**, 1–13 (2016).
- 455 20. Sun, D. M. *et al.* Flexible high-performance carbon nanotube integrated circuits. *Nat.*
456 *Nanotechnol.* **6**, 156–161 (2011).

- 457 21. Wang, C. *et al.* Extremely bendable, high-performance integrated circuits using
458 semiconducting carbon nanotube networks for digital, analog, and radio-frequency
459 applications. *Nano Lett.* **12**, 1527–1533 (2012).
- 460 22. Wang, C., Zhang, J. & Zhou, C. Macroelectronic integrated circuits using high-
461 performance separated carbon nanotube thin-film transistors. *ACS Nano* **4**, 7123–7132
462 (2010).
- 463 23. Zhu, C. *et al.* Stretchable temperature-sensing circuits with strain suppression based on
464 carbon nanotube transistors. *Nat. Electron.* **1**, 183–190 (2018).
- 465 24. Sun, D. M. *et al.* Mouldable all-carbon integrated circuits. *Nat. Commun.* **4**, 1–8 (2013).
- 466 25. Hirotani, J., Kishimoto, S. & Ohno, Y. Origins of the variability of the electrical
467 characteristics of solution-processed carbon nanotube thin-film transistors and
468 integrated circuits. *Nanoscale Adv.* **1**, 636–642 (2018).
- 469 26. Chen, J. & Kumar, S. Variability in output characteristics of single-walled carbon
470 nanotube thin-film transistors. *IEEE Trans. Nanotechnol.* **17**, 353–361 (2018).
- 471 27. Zhang, Z. *et al.* Self-aligned ballistic n-type single-walled carbon nanotube field-effect
472 transistors with adjustable threshold voltage. *Nano Lett.* **8**, 3696–3701 (2008).
- 473 28. Chen, B. *et al.* Highly uniform carbon nanotube field-effect transistors and medium
474 scale integrated circuits. *Nano Lett.* **16**, 5120–5128 (2016).
- 475 29. Lei, T. *et al.* Low-voltage high-performance flexible digital and analog circuits based
476 on ultrahigh-purity semiconducting carbon nanotubes. *Nat. Commun.* **10**, 2161 (2019).
- 477 30. Wang, B.-W. *et al.* Continuous fabrication of meter-scale single-wall carbon nanotube
478 films and their use in flexible and transparent integrated circuits. *Adv. Mater.* **30**,
479 1802057 (2018).
- 480 31. Shao, L. *et al.* Compact modeling of thin film transistors for flexible hybrid IoT design.
481 *IEEE Des. Test* **36**, 6–14 (2019).

- 482 32. Salvatore, G. A. *et al.* Wafer-scale design of lightweight and transparent electronics that
483 wraps around hairs. *Nat. Commun.* **5**, 2982 (2014).
- 484 33. Garripoli, C. *et al.* Analogue frontend amplifiers for bio-potential measurements
485 manufactured with a-IGZO TFTs on flexible substrate. *IEEE J. Emerg. Sel. Top.*
486 *Circuits Syst.* **7**, 60–70 (2017).
- 487 34. Papadopoulos, N. *et al.* In-panel 31.17dB 140kHz 87 μ W unipolar dual-gate In-Ga-Zn-
488 O charge-sense amplifier for 500dpi sensor array on flexible displays. in *IEEE 44th*
489 *European Solid State Circuits Conference (ESSCIRC), Dresden, Germany, 3–6*
490 *September 2018*, 102–105 (IEEE, 2018).
- 491 35. Marien, H., Steyaert, M. S. J., Van Veenendaal, E. & Heremans, P. Analog building
492 blocks for organic smart sensor systems in organic thin-film transistor technology on
493 flexible plastic foil. *IEEE J. Solid-State Circuits* **47**, 1712–1720 (2012).
- 494 36. Nausieda, I. *et al.* Mixed-signal organic integrated circuits in a fully photolithographic
495 dual threshold voltage technology. *IEEE Trans. Electron Devices* **58**, 865–873 (2011).
- 496 37. Chang, J., Zhang, X., Ge, T. & Zhou, J. Fully printed electronics on flexible substrates:
497 High gain amplifiers and DAC. *Org. Electron.* **15**, 701–710 (2014).
- 498 38. Torres-Miranda, M. *et al.* High-speed plastic integrated circuits: Process integration,
499 design, and test. *IEEE J. Emerg. Sel. Top. Circuits Syst.* **7**, 1–14 (2016).
- 500 39. Sugiyama, M. *et al.* An ultraflexible organic differential amplifier for recording
501 electrocardiograms. *Nat. Electron.* **2**, 351–360 (2019).
- 502 40. Ishida, K. *et al.* 22.5 dB open-loop gain, 31 kHz GBW pseudo-CMOS based operational
503 amplifier with a-IGZO TFTs on a flexible film. in *2014 IEEE Asian Solid-State Circuits*
504 *Conference, KaoHsiung, Taiwan, 10–12 November 2014*, 313–316 (IEEE, 2015).
- 505 41. Zysset, C. *et al.* IGZO TFT-based all-enhancement operational amplifier bent to a radius
506 of 5 mm. *IEEE Electron Device Lett.* **34**, 1394–1396 (2013).

- 507 42. Shabanpour, R. *et al.* A 70° phase margin OPAMP with positive feedback in flexible a-
508 IGZO TFT technology. in *2015 IEEE 58th International Midwest Symposium on*
509 *Circuits and Systems (MWSCAS), Fort Collins, CO, USA, 2–5 August 2015*, 13–16
510 (IEEE, 2015).
- 511 43. Kim, D., Kim, Y., Choi, K. Y., Lee, D. & Lee, H. A solution-processed operational
512 amplifier using direct light-patterned a-InGaZnO TFTs. *IEEE Trans. Electron Devices*
513 **65**, 1796–1802 (2018).
- 514 44. Rahaman, A., Chen, Y., Hasan, M. M. & Jang, J. A high performance operational
515 amplifier using coplanar dual gate a-IGZO TFTs. *IEEE J. Electron Devices Soc.* **7**, 655–
516 661 (2019).
- 517 45. Kim, K., Choi, K. Y. & Lee, H. a-InGaZnO thin-film transistor-based operational
518 amplifier for an adaptive DC-DC converter in display driving systems. *IEEE Trans.*
519 *Electron Devices* **62**, 1189–1194 (2015).
- 520 46. Tarn, Y. C., Ku, P. C., Hsieh, H. H. & Lu, L. H. An amorphous-silicon operational
521 amplifier and its application to a 4-bit digital-to-analog converter. *IEEE J. Solid-State*
522 *Circuits* **45**, 1028–1035 (2010).
- 523 47. Chen, Z. J. *et al.* A new high-gain operational amplifier using transconductance-
524 enhancement topology integrated with metal oxide TFTs. *IEEE J. Electron Devices Soc.*
525 **7**, 118–126 (2019).
- 526 48. Chantaf, S., Naït-Ali, A., Karasinski, P. & Khalil, M. ECG modelling using wavelet
527 networks: Application to biometrics. *Int. J. Biom.* **2**, 236–249 (2010).
- 528 49. Myny, K. The development of flexible integrated circuits based on thin-film transistors.
529 *Nat. Electron.* **1**, 30–39 (2018).
- 530 50. Deen, M. J., Marinov, O., Zschieschang, U. & Klauk, H. Organic thin-film transistors:
531 Part II-parameter extraction. *IEEE Trans. Electron Devices* **56**, 2962–2968 (2009).

532

533 **Acknowledgement**

534 This work was partially supported by the Japan Science and Technology Agency CREST
535 program (JPMJCR16Q2), MEXT KAKENHI (Grant Number JP15H05867), and JSPS
536 KAKENHI (Grant Number JP20H00243).

537 **Author contributions**

538 Y.O. conceived and supervised this work. T.K. designed and performed the experiments. H.K.
539 prepared the purified semiconducting CNTs. S.K. designed the nichrome resistors. T.K. and
540 Y.O. co-wrote the paper. All authors discussed the results and commented on the manuscript.

541 **Conflicts of interest**

542 The authors have no conflicts of interest to declare.

543

Figures

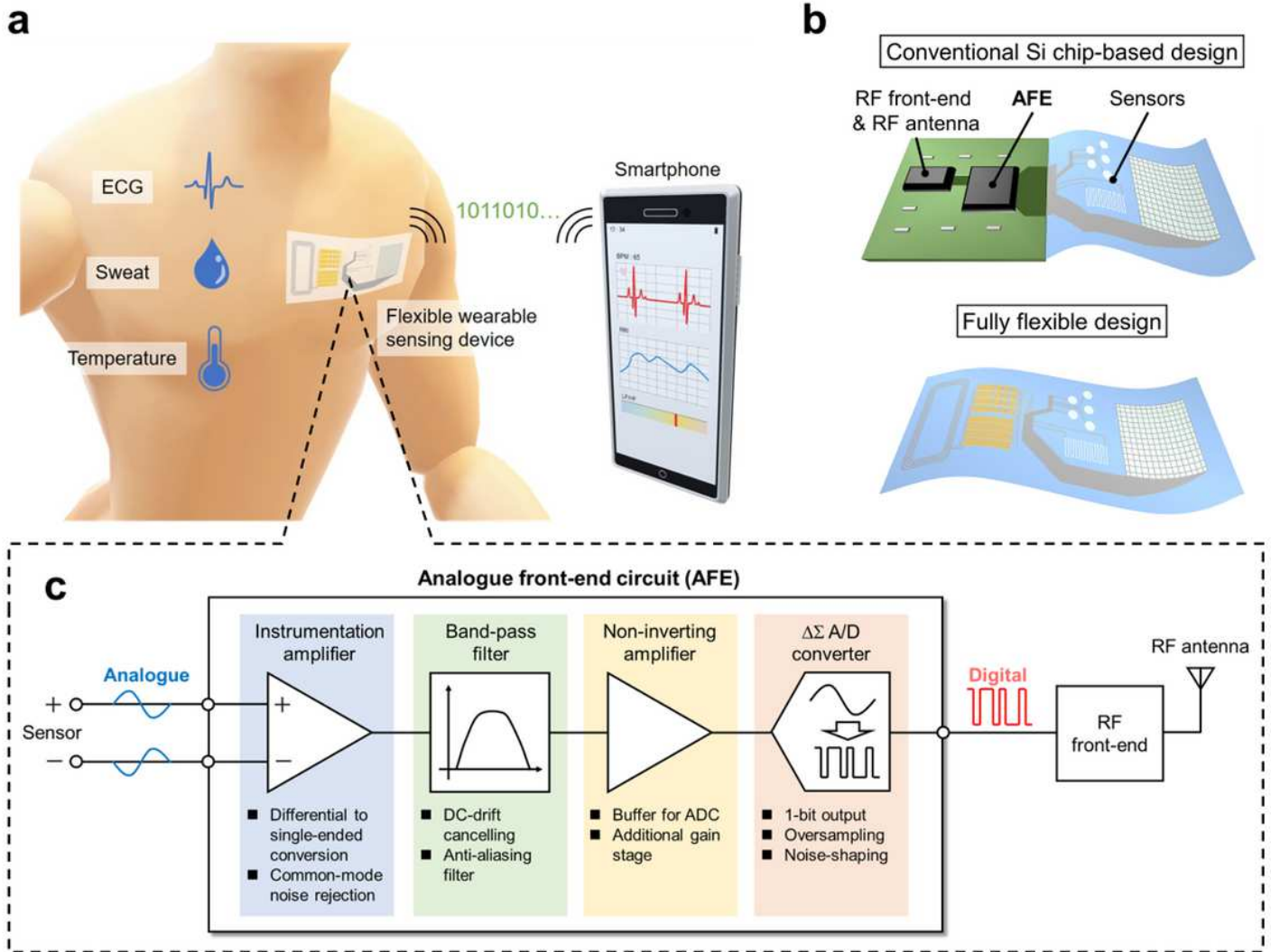


Figure 1

Fully flexible electronics for epidermal sensors. (a) Schematic illustration of an epidermal sensor for monitoring biological signals. (b) Schematic illustrations of a conventional Si chip-based design and fully flexible design of flexible sensor. (c) Circuit diagram of the sensor system consisting of a sensor, AFE, and RF frontend. The configuration of the AFE and roles of each element are also shown.

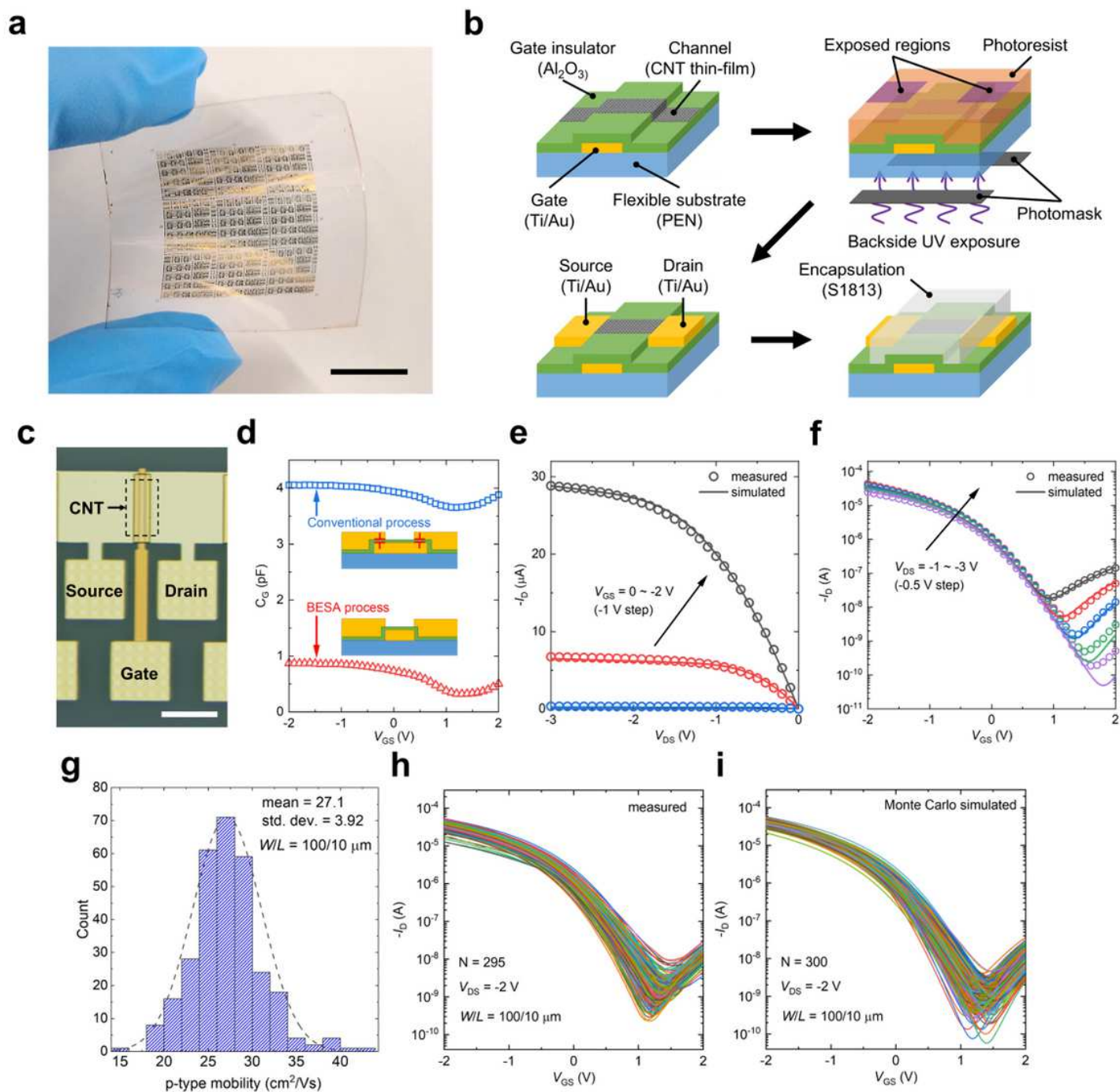


Figure 2

Flexible CNT TFTs fabricated with the BESA process. (a) Photograph of devices fabricated on a PEN film. The scale bar is 1 cm. (b) Schematic illustration of the device fabricated with the BESA process. (c) Photograph of a CNT TFT. (d) CG-VGS characteristics of CNT TFTs fabricated by the conventional process and BESA process. (e) ID-VDS and (f) ID-VGS characteristics of a typical CNT TFT. (g) Histogram of carrier mobility. The broken curve is the Gaussian fit. The mean value and standard deviation were 27.1 and 3.92 cm^2/Vs . (h) Measured and (i) simulated ID-VGS characteristics of CNT TFTs at $V_{DS} = -2$ V.

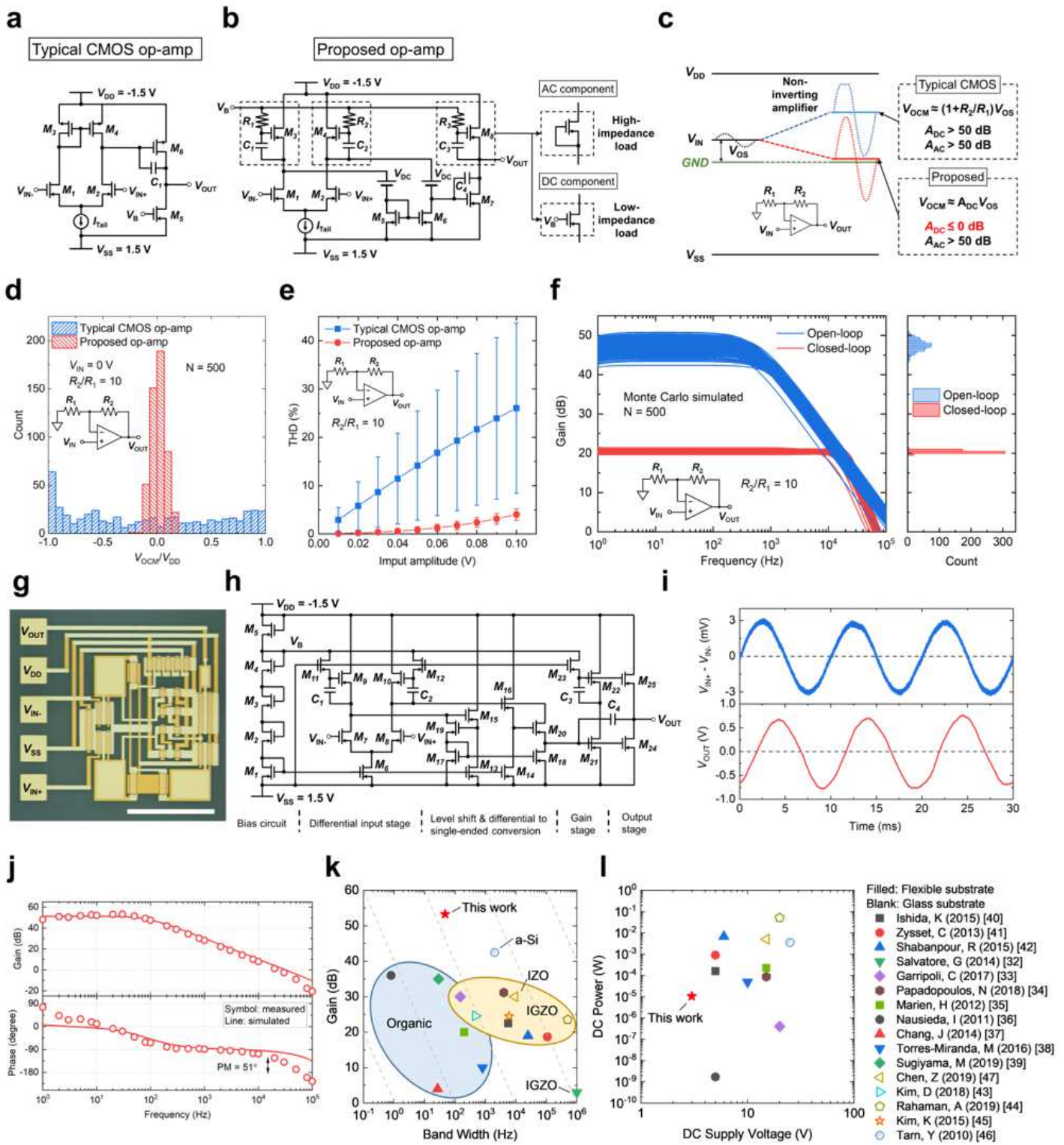


Figure 3

Design and fabrication of the high-gain and low-voltage op-amp with high tolerance to transistor variability. (a) Circuit configuration of a typical two-stage CMOS-based op-amp. (b) Circuit configuration of the proposed op-amp. (c) Schematics of the voltage levels of V_{OS} and V_{OCM} for non-inverting amplifiers composed of the CMOS-based op-amp and proposed op-amp, respectively. The inset shows the circuit configuration of the non-inverting amplifier. Results of the Monte Carlo simulations of op-

amps: (d) VOCM distribution normalised by VDD, (e) THD as a function of the input voltage amplitude of non-inverting amplifiers composed of the CMOS op-amp and proposed op-amp, and (f) open-loop voltage gain of the proposed op-amp and closed-loop voltage gain of the non-inverting amplifier composed of the proposed op-amp as functions of the frequency and the maximum gain distributions. (g) Photograph of the fabricated flexible CNT op-amp. The scale bar is 500 μm . (h) Circuit diagram of the CNT op-amp. (i) Input (upper) and output (bottom) voltage waveforms. (j) Fabrication and characterisation of the CNT op-amp. (k) Voltage gain versus bandwidth and (l) DC power versus DC supply voltage of the present CNT op-amp and the differential amplifiers and op-amps reported previously for comparison.

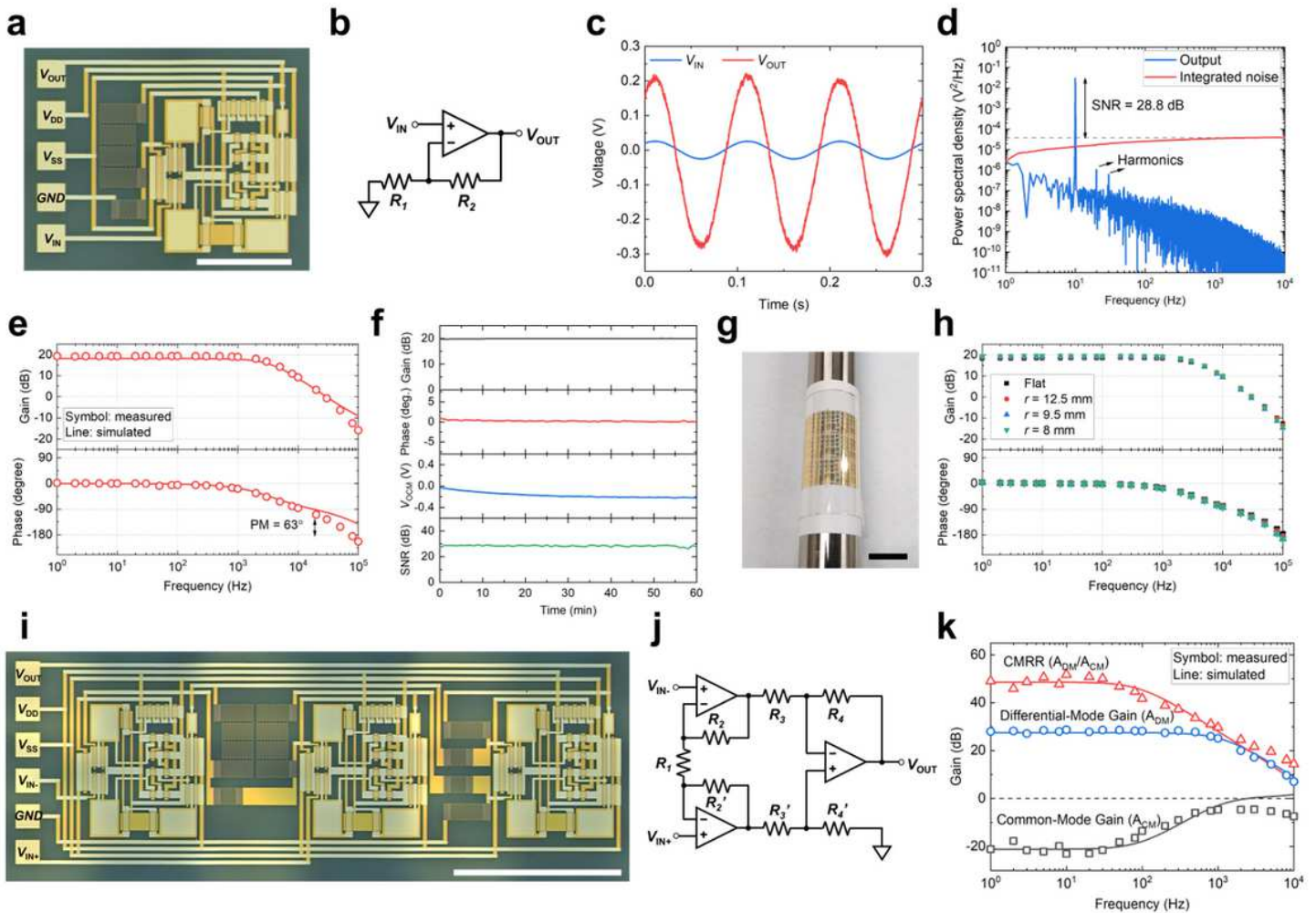


Figure 4

Negative-feedback circuits composed of CNT op-amps. Non-inverting amplifier: (a) photograph (scale bar: 500 μm), (b) circuit diagram, (c) input and output voltage waveform, (d) power spectral density as a function of frequency, (e) measured (open circle) and simulated (solid curve) gain (upper) and phase (bottom) as a function of frequency, and (f) changes in the gain, phase, VOCM, and SNR (from top to bottom) for 1 h. (g) Photograph of the bending test (scale bar: 1 cm), and (h) gain and phase as a function of frequency under various bending condition. Instrumentation amplifier: (i) photograph, (j) circuit diagram, and (k) CMRR, ADM, and ACM as a function of frequency.

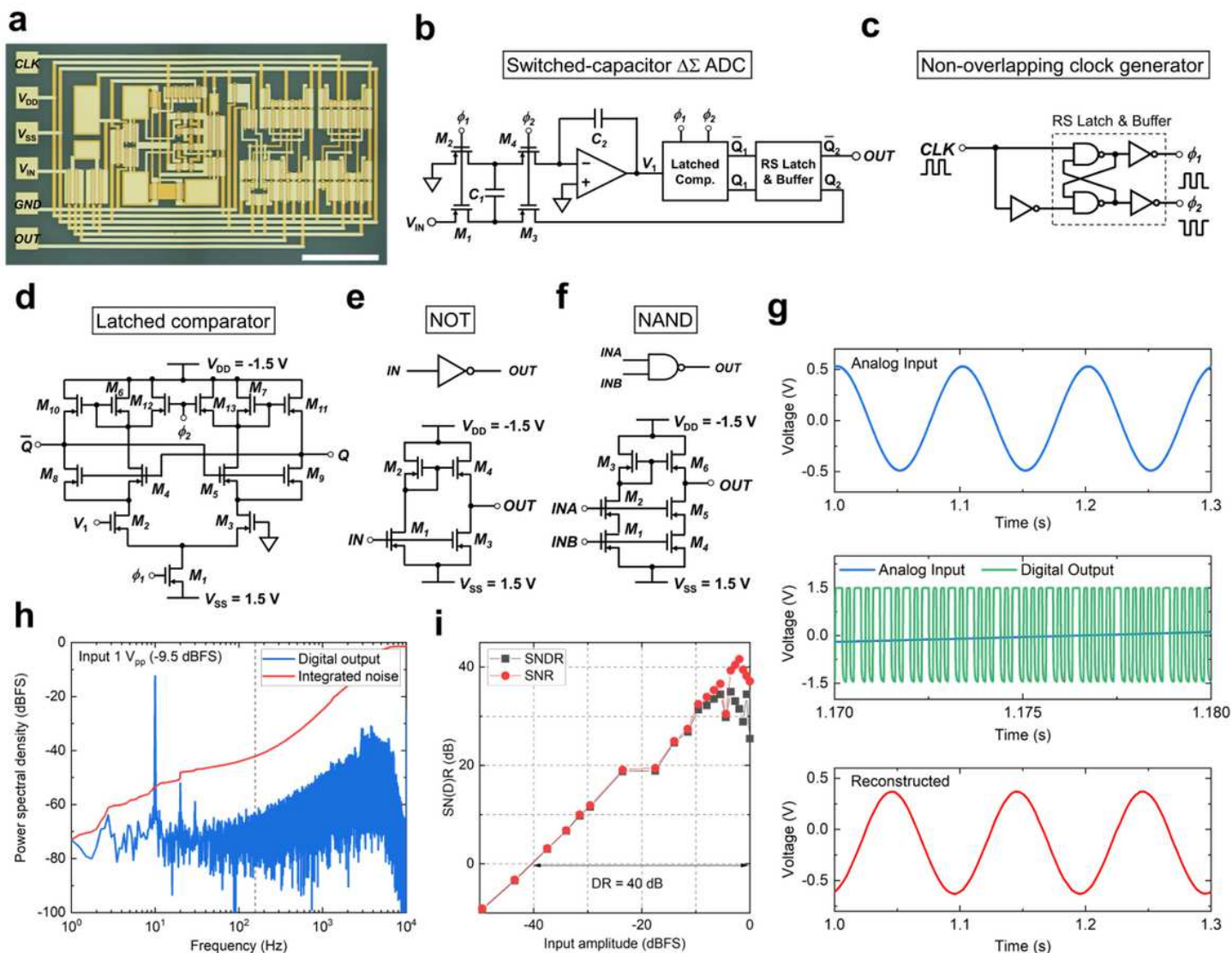


Figure 5

Flexible CNT ADC. (a) Photograph (Scale bar: 500 μm) and (b) circuit diagram of SC $\Delta\Sigma$ ADC fabricated in this study. Circuit diagrams of the (c) non-overlapping clock generator, (d) latched capacitor, (e) NOT gate, and (f) NAND gate. (g) Input voltage (top), analogue input voltage and digital output voltage on a magnified time scale (middle), and analogue signal reconstructed from the digital output (bottom). (h) PSD and integrated noise level of the digital output as a function of the frequency. (i) SNR and SNDR versus the input voltage amplitude.

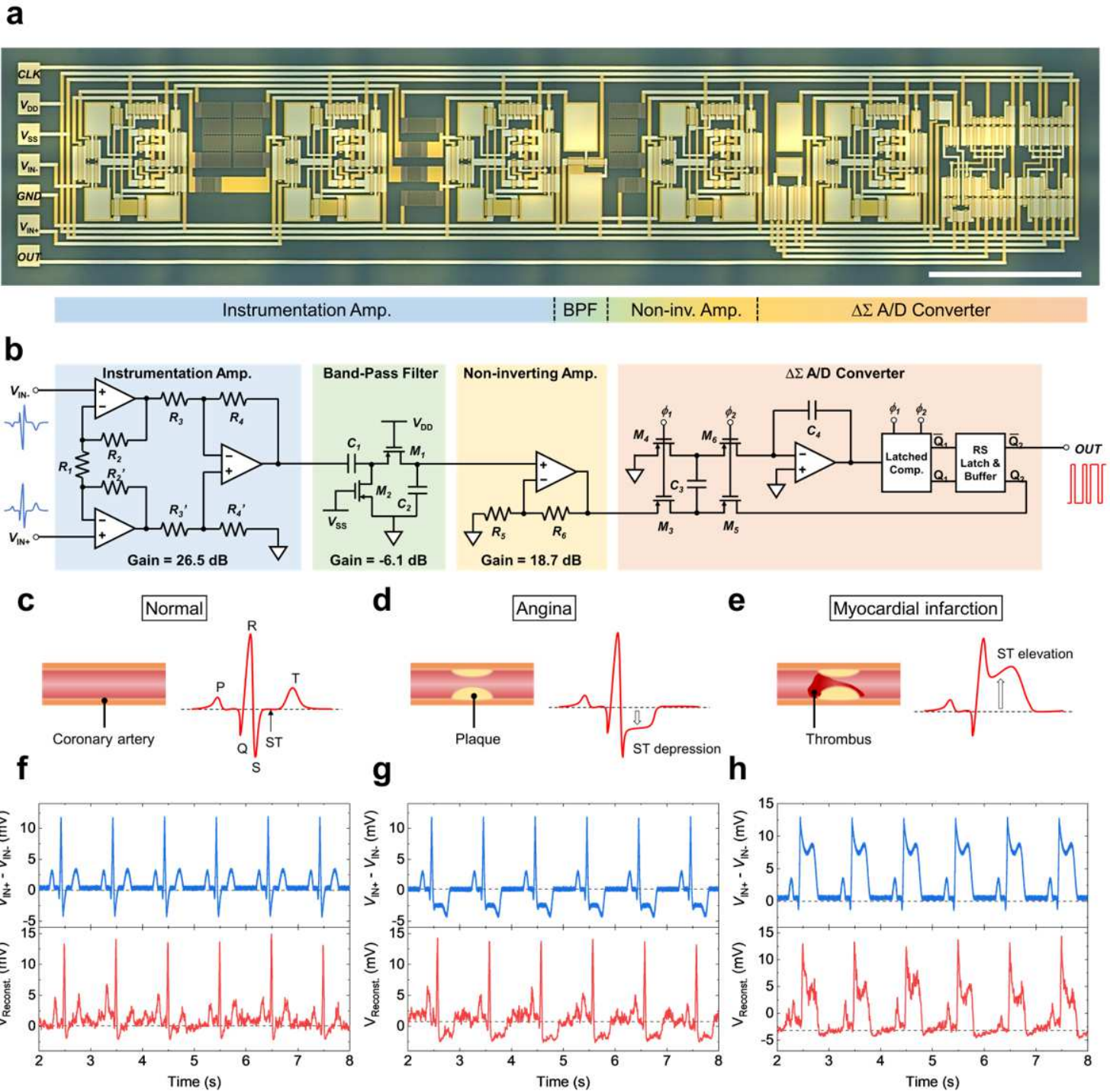


Figure 6

CNT-based fully flexible AFE. (a) Photograph (scale bar: 1 mm) and (b) block diagram. Schematics of the coronary artery and ECG waveforms indicating (c) normal conditions, (b) an angina, and (c) a myocardial infarction (c). Input voltage waveforms to the AFM (upper) and reconstructed voltage waveforms from the digital output data (bottom) indicating (f) normal conditions, (g) an angina, and (h) a myocardial infarction.

Supplementary Files

This is a list of supplementary files associated with this preprint. Click to download.

- [SupplementrayInformation200830submitted.docx](#)